Insights into the Nature and Evolution upon Electrochemical Cycling of Planar Defects in the β-$NaMnO_2$ Na-ion Battery Cathode: An NMR and First-Principles Density Functional Theory Approach

Supplementary Information

Raphaële J. Clément,[a] Derek S. Middlemiss,[a, b] Ieuan D. Seymour,[a] Andrew J. Ilott,[c, d] Clare P. Grey[a, d]

[a] Department of Chemistry, University of Cambridge, Cambridge, CB2 1EW, U.K.

[b] Department of Chemistry, University of Warwick, Coventry, CV4 7AL, U.K.

[c] Department of Chemistry, New York University, New York, NY 10003, United States

[d] Department of Chemistry, Stony Brook University, Stony Brook, NY 11790-3400, United States

1. Additional computational details

1.1. CRYSTAL09 calculations

All-electron atom-centered basis sets comprising fixed contractions of Gaussian primitive functions were employed throughout. Two spin-polarized exchange-correlation functionals based upon the B3LYP form,[1-4] and with Fock exchange weights of F_0 = 20 % (B3LYP or H20) and 35 % (H35), were chosen for their good performance for the electronic structure and band gaps of transition metal compounds (B3LYP or H20),[5,6] and for their accurate description of the magnetic properties of related compounds (H35)[7-9]. Besides, previous studies have shown that the hyperfine shifts calculated with the H20 and the H35 functionals on similar compounds are in good agreement with experiment.[10-12] Two types of basis sets were used: a smaller basis set (BS–I) was employed for structure optimizations, and a larger basis set (BS–II) was used to compute the ^{23}Na NMR parameters which require an accurate description of the occupation of core-like electronic states. For BS–I, individual atomic sets were of the form (15s7p)/[1s3sp] for Na, (20s12p5d)/[1s4sp2d] for Mn, (10s4p1d)/[1s2sp1d] for O, where the values in parentheses denote the number of Gaussian primitives and the values in square brackets the contraction scheme. All BS–I sets were obtained from the CRYSTAL online repository and were unmodified from their previous use in a broad range of compounds.[13] For BS–II, a modified IGLO-III (10s6p2d)/[6s5p2d] set was adopted for O, a flexible and extended TZDP-derived (11s7p)/[7s3p] set was used for Na, and an Ahlrichs DZP-derived (13s9p5d)/[7s5p3d] set was applied to Mn[14]. The Mn and O BS–II sets are consistent with those used in a recent calculation of hyperfine parameters in lithium transition metal phosphates.[12]

^{23}Na NMR parameters were computed in the experimentally determined[15,16] (EXP) and in the fully optimized (i.e. relaxed atomic positions and cell parameters; OPT) α- and β-$NaMnO_2$ structures, and in supercells containing twin planes between local ‘α-like’ and ‘β-like’ domains. First-principles structure optimizations were carried out in the ferromagnetic (FM) state, after removal of all symmetry constraints (within the P1 space group). Structure optimizations were pursued using the quasi-Newton algorithm with RMS convergence tolerances of 10^{-7}, 0.0003, and 0.0012 au for total energy, root-mean-square (rms) force, and rms displacement, respectively. Tolerances for maximum force and displacement components were set at 1.5 times the respective rms values. Sufficient convergence in total energies and spin densities was obtained by application of integral series truncation thresholds of 10^{-7}, 10^{-7}, 10^{-7}, 10^{-7}, and 10^{-14} for Coulomb overlap and penetration, exchange overlap, and g- and n-series exchange penetration, respectively, as defined in the CRYSTAL documentation.[13] The

final total energies and spin and charge distributions were obtained in the absence of any spin and eigenvalue constraints. NMR parameters for the different Na sites were obtained in the experimental and optimized ferromagnetic geometries, using BS-II sets and a method identical to that described in Middlemiss et al.'s recent work.[11]

Anisotropic Monkhorst-Pack[17] reciprocal space meshes with sets of shrinking factors (12, 12, 8) and (12, 6, 8), were used to optimize the α-$NaMnO_2$ and β-$NaMnO_2$ unit cells, starting from the experimental structures by Parant et al.[15] and Hoppe et al.[16] The lattice parameters for the α- and β-$NaMnO_2$ structures relaxed using the H20 and H35 functionals are compared to the experimental unit cell parameters in Table S1.

Polymorph	Structure	*a* / Å	*b* / Å	*c* / Å	α / °	β / °	γ / °	V / Å^3
α-$NaMnO_2$ (*C2/m*)	EXP[15]	3.16	3.16	5.77	69.7	110.3	126.1	42.79
	OPT H20	3.09	3.09	5.53	70.5	109.5	125.0	40.06
	OPT H35	3.07	3.07	5.51	70.6	109.4	124.8	39.47
β-$NaMnO_2$ (*Pmnm*)	EXP[16]	2.86	6.34	4.79	90.0	90.0	90.0	86.71
	OPT H20	2.85	6.29	4.68	90.0	90.0	90.0	83.81
	OPT H35	2.84	6.28	4.64	90.0	90.0	90.0	82.73

Table S1. Unit cell parameters obtained by Parant et al.[15] and Hoppe et al.[16] for the experimental α- and β-$NaMnO_2$ structures, respectively, and for the α- and β-$NaMnO_2$ structures optimized using the H20 and H35 functionals.

An isotropic Monkhorst-Pack reciprocal space mesh with shrinking factor 4 was used for the hyperfine and spin flip calculations on a $(4a + 4c, 4b, 2c)$ expansion of the *C2/m* unit cell of α-$NaMnO_2$ and on a $(2a + 2c, 2b, -2a + 2c)$ expansion of the *Pmnm* unit cell of β-$NaMnO_2$. The symmetry was removed after the cell expansion to allow for individual spin flips. A (4, 2, 1) Monkhorst-Pack mesh was used for Mixed Cell 1, with lattice parameters close to a = 5.70 Å, b = 12.58 Å, and c = 23.38 Å. A (4, 4, 2) Monkhorst-Pack mesh was used for Mixed Cell 2, with lattice parameters of a = 5.70 Å, b = 6.29 Å, and c = 18.70 Å.

1.2. VASP5.2 calculations

Formation energies and deintercalation potentials were computed on $NaMnO_2$-type structures using a standard PAW potential for O, while the 2p semi-core states were treated as valence states for both Na and Mn. Anisotropic Monkhorst-Pack[17] k-point meshes of (6, 12, 10) and (12, 6, 10) were selected for calculations within two formula unit cells of the α-$NaMnO_2$ and β-

$NaMnO_2$ end member compounds, respectively. k-point meshes of (2, 6, 3) and (6, 3, 2) were used for the calculations of intercalation potentials in 40 formula unit supercells of α- and β-$NaMnO_2$. A (6, 3, 2) k-point mesh was also used for calculations on the Mixed Cell 1 structure containing 40 formula units. The threshold differences in the total free energy for self-consistent field (SCF) and for geometry convergence were set to 5×10^{-6}eV and 1×10^{-5} eV, respectively. A small Gaussian-type smearing of the Fermi level, equivalent to a temperature of 11.6 K, was applied. Localization of the Mn^{4+} charge in partially deintercalated cells was achieved by setting the initial magnetic moment for each atom to its desired value. The total magnetization of the cell was fixed to the value corresponding to the initial magnetic spin configuration in the first structure optimization run. The total cell magnetization constraint was released in a subsequent structure optimization run. The charge density was recalculated at the start of each new optimization and single point energy run from the wavefunction obtained at the end of the previous run. The final energies, and spin and charge distributions of the different configurations were obtained from a single point energy run in the absence of magnetic constraints. The final Mn charges were determined from local magnetic moments integrated over spheres of Wigner-Seitz radius of 1.323 Å centered at each Mn position in the cell. Local magnetic moments for Mn^{3+} ions were in the range 3.77-3.79 μ_B, while a 3.05 μ_B magnetic moment was obtained for Mn^{4+} ions.

2. $NaMnO_2$-type structures considered in this work

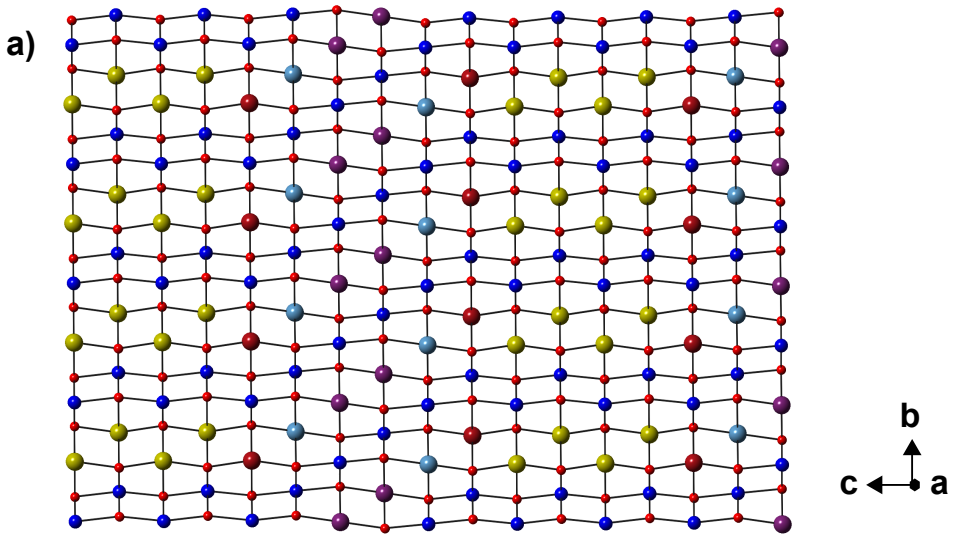

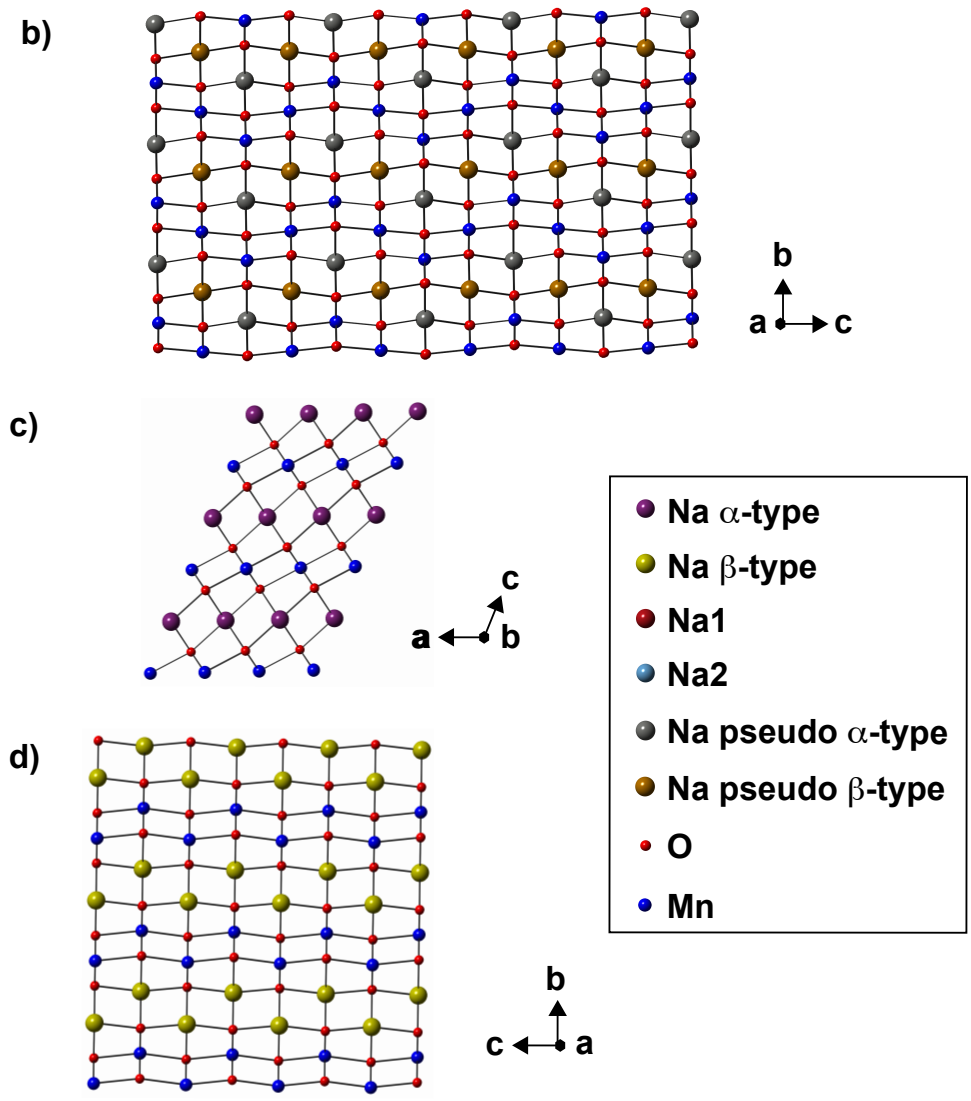

Figure S1. Diagrams of the two mixed α/β-$NaMnO_2$ structures considered here with twin boundaries between α and β domains: a) Mixed Cell 1, and b) Mixed Cell 2. The structures of the ideal c) α-$NaMnO_2$ and d) β-$NaMnO_2$ polymorphs are shown for comparison.

3. First-principles magnetic coupling constants for α- and β-$NaMnO_2$

3.1. Methodology

The three nearest-neighbor J_a magnetic coupling constants between pairs of Mn^{3+} spins considered here for α- and β-$NaMnO_2$ are depicted in Figure S2.

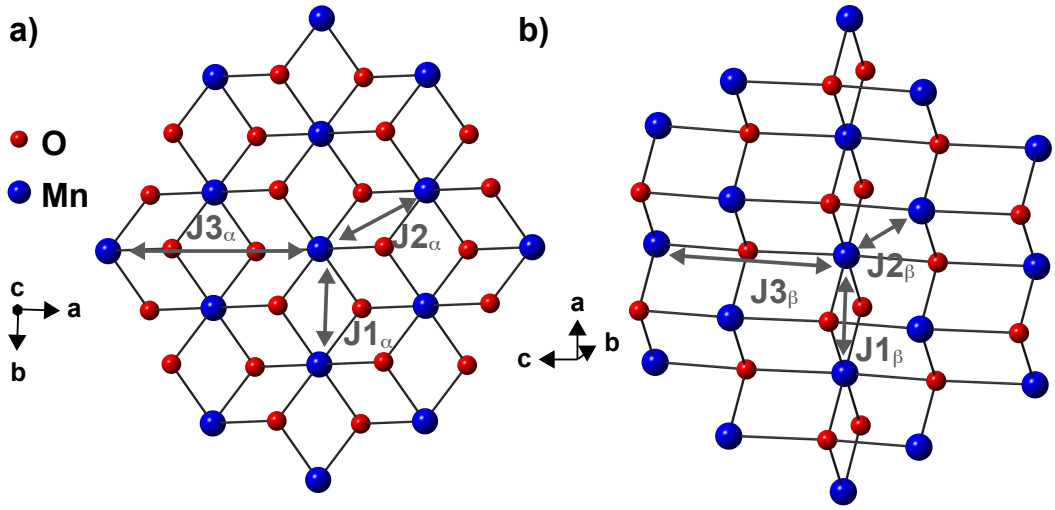

Figure S2. The three nearest neighbor in plane Mn^{3+}…Mn^{3+} magnetic interactions for a) α-$NaMnO_2$, and b) β-$NaMnO_2$.

Exchange couplings were evaluated from the first-principles energy difference between the purely ferromagnetic cell (E_{ferro}) and carefully selected sets of spin configurations wherein individual and pairs of Mn spins were flipped (E_{mag}),

$$E_{\mathrm{mag}} - E_{\mathrm{ferro}} = 2\sum_{a} J_a \sum_{i,j\in a} S_i S_j \qquad \text{(S1)},$$

where the sum is made over all i, j spin pairs with formal spins S_i and S_j, in antiferromagnetic configurations for each interaction type, without double counting. The factor of 2 is present because the energy is defined relative to the purely ferromagnetic state. This results in a set of linear equations that were solved simultaneously to yield the different J_a values. Within the sign convention applied here, positive J_a values correspond to ferromagnetic interactions between the spins, while negative J_a values correspond to antiferromagnetic interactions. The calculations were performed on supercells of α- and β-$NaMnO_2$ containing 32 formula units.

3.2. Results

J_α and J_β coupling constants depicted above were evaluated in the experimental (EXP) and optimized (OPT) α- and β-$NaMnO_2$ structures, respectively. In each structure investigated, two calculations were performed using the H20 and H35 hybrid correlation-exchange functionals and the results are shown in Table S2. In the table below, $J'_{3\alpha}$ and $J'_{3\beta}$ denote magnetic interactions across the twin plane boundary between α and β nanodomains. These exchange

couplings were computed on the optimized Mixed Cell 1 structure (see Figure 2a in the main text) and are structurally similar to the $J_{3\alpha}$ and $J_{3\beta}$ interactions in α- and β-$NaMnO_2$.

Exchange coupling	H20 / K	H35 / K	d(Mn…Mn) / Å	Mn-O-Mn / °
$J_{1\alpha}$ (z_a = 2)	-62.03 (-55.66)	-49.35 (-45.45)	2.85 (2.86)	2 x 95.7 (2 x 93.5)
$J_{2\alpha}$ (z_a = 4)	-8.12 (-5.29)	-1.06 (0.30)	3.09 (3.16)	2 x 94.6 (2 x 95.2)
$J_{3\alpha}$ (z_a = 2)	-0.36 (-0.54)	-0.18 (-0.31)	5.48 (5.63)	Long range
$J'_{3\alpha}$ (z_a = 2)	-0.24	-0.11	5.57	Long range
$J_{1\beta}$ (z_a = 2)	-60.17 (-56.60)	-47.43 (-44.44)	2.85 (2.86)	95.2 & 96.5 (94.5 & 96.4)
$J_{2\beta}$ (z_a = 4)	-2.93 (-2.16)	1.74 (1.88)	3.15 (3.22)	2 x 94.3 (2 x 94.6)
$J_{3\beta}$ (z_a = 2)	-34.38 (-28.38)	-25.35 (-19.34)	4.68 (4.79)	167.4 (166.6)
$J'_{3\beta}$ (z_a = 2)	-34.63	-25.64	4.68	168.2

Table S2. First-principles magnetic exchange coupling constants (J_a) for the three nearest-neighbor interactions obtained on the various $NaMnO_2$ structures optimized using the H20 and H35 hybrid correlation-exchange functionals (F_0 = 20 and 35 %). A description of the different magnetic interaction pathways is given here for the H20 optimized (OPT) structures. The coupling constants obtained on the experimental (EXP) structures and their geometrical parameters are presented in brackets. z_a is the number of neighboring Mn spins in the a^{th} shell around the central spin.

The J_1 magnetic exchange interactions perpendicular to the Jahn-Teller axis (or ferro-orbital ordering direction) are largest in both α- and β-$NaMnO_2$, in good agreement with previous experimental reports.[18-22] The Mn spin lattice is described hereafter by zigzag chains running along the J_1 (intrachain) interactions in the MnO_2 plane, with weaker interchain couplings in the MnO_2 plane and between adjacent MnO_2 planes (interplane). The J_1 and J_2 magnetic couplings proceed via two approximately 90° Mn-O-Mn interaction pathways. The intrachain J_1 interaction involves four Jahn-Teller shortened Mn-O bonds, while the interchain J_2 coupling involves two shortened and two elongated bonds. The nearest-neighbor interaction

with the 2nd adjacent chain in the MnO_2 plane, J_3, is different in the α and β forms. In β-$NaMnO_2$ it proceeds via an approximately 180° Mn-O-Mn interaction pathway and two Jahn-Teller elongated Mn-O bonds. Such an interaction is not present in α-$NaMnO_2$, and instead $J_{3\alpha}$ corresponds to a long-range magnetic coupling to the 2nd adjacent chain (d(Mn…Mn) = 5.48 Å). Longer-range intraplane and interplane interactions were found to be weak (< 1.8 K in magnitude, not shown here). Our calculations on Mixed Cell 1 yield $J'_{3\alpha}$ and $J'_{3\beta}$ values within 0.3 K of the $J_{3\alpha}$ and $J_{3\beta}$ interactions (OPT) presented in Table S2, indicating that the presence of a twin boundary between the two polymorphs of $NaMnO_2$ has a minimal effect on the J_a couplings. For simplicity, the $J_{1\alpha}, J_{2\alpha}, J_{3\alpha}$ and $J_{1\beta}, J_{2\beta}, J_{3\beta}$ values were used in the magnetic Monte Carlo simulations.

3.3. Comparison to literature values

In their neutron powder diffraction and magnetic susceptibility study, Giot et al. predicted a dominant exchange interaction, J_1, and a small J_2/J_1 ratio,[18] and a later Lanczos fit of the experimental magnetic susceptibility data yielded a J_2/J_1 ratio of 0.44.[19] On the other hand, Stock et al.[20] were able to obtain a good fit of low-temperature Neutron Inelastic Scattering (NIS) data using a 1D magnetic model, with a $J_1 = 73 \pm 5$ K and a sizeable single-ion anisotropy. The discrepancy between the low temperature (NIS) vs. high temperature (Lanczos fit) results may arise from the different time domains probed with the different characterization techniques, as suggested by the authors of the NIS study.[20] It may also be argued that Lanczos fits of magnetic susceptibility data are not as reliable as fits of low temperature NIS studies, since dynamic effects become significant at higher temperature.

When it comes to first-principles computations, hybrid functionals (and to a lesser extent the GGA+U method) have been found to provide coupling constants of better accuracy than pure density functional across a wide range of materials.[23] The hybrid DFT results shown here are in agreement with Stock et al.'s experimental findings and yield small J_2/J_1 ratios, comprised between -0.01 (H35) and 0.13 (H20), for α-$NaMnO_2$. These ratios are smaller than previous first-principles studies on α-$NaMnO_2$. For instance, Zhang et al.'s GGA and GGA+U calculations (using a $U_{eff} = 8.8$ eV) yielded J_2/J_1 ratios of 0.33 and 0.18, respectively.[24] Abakumov et al. obtained $J_1 = 72$ K and $J_2 = 23$ K (i.e. J_2/J_1=0.32) for α-$NaMnO_2$, and $J_1 = 70$ K and $J_3 = 57$ K for β-$NaMnO_2$ using GGA+U but a somewhat small $U_{eff} = 2.0$ eV chosen to reproduce the magnetic couplings of α-$NaMnO_2$.[21]

Finally, the discrepancy between the first-principles J_2/J_1 ratios presented here and obtained from calculations on stoichiometric $NaMnO_2$ and those obtained experimentally data Lanczos fit of high temperature susceptibility data[19] may be accounted for by the presence of Mn^{4+} defects in the real material. Even low concentrations of these defects are expected to increase the strength of the J_2 exchange coupling, hence the J_2/J_1 ratio. Additional first-principles calculations (not shown here) suggest that the oxidation of one of the interacting manganese, from Mn^{3+} to Mn^{4+}, has a large effect on the J_2 coupling, which goes from being small and negative (AFM), to relatively large and positive (FM).

4. Evaluating bulk and site-specific magnetic scaling factors

4.1. Bulk scaling factor from experimental magnetic susceptibility measurements

The bulk magnetic susceptibility of the as-synthesized β-$NaMnO_2$ sample, shown in Figure S3, is in good agreement with a previous report[21] and exhibits a broad maximum at room temperature, consistent with strong remnant 2D antiferromagnetic correlations. The three sets of data shown below were recorded on three different samples of β-$NaMnO_2$, i.e. containing a different proportion of twin planes and α domains. This leads to slightly different magnetic susceptibility curves, since the magnetic couplings in α and β domains, and in the vicinity of the twin boundaries are different. This observation further demonstrates the importance of considering local magnetic susceptibilities to understand the NMR response of the various Na nuclei in the disordered material. A linear fit of the inverse susceptibility $1/\chi$ vs. T curve, over the temperature $600 \leq T \leq 700$ yields a Weiss constant Θ = - 487 K (r^2= 0.999), in excellent agreement with the - 490 K value reported for α-$NaMnO_2$.[20]

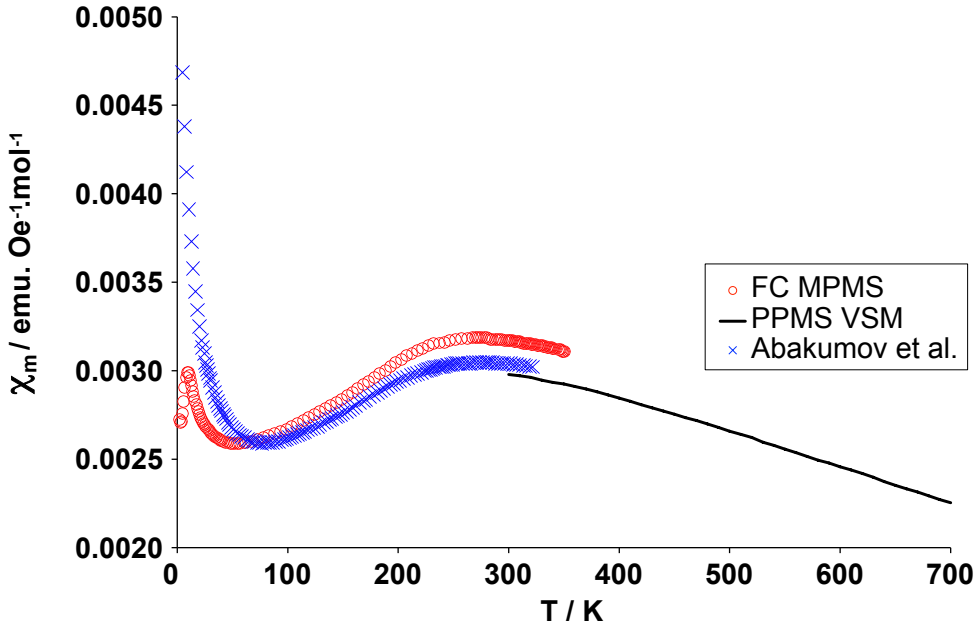

Figure S3. Experimental molar magnetic susceptibility vs. temperature curves for three different samples of β-$NaMnO_2$. The field cooled data (red circles) and the high temperature data (black line) were obtained at 0.1 T on an MPMS and on a PPMS equipped with a VSM oven, respectively. The data shown with blue crosses are adapted with permission from Abakumov et al.[21] Copyright 2014 American Chemical Society.

A 'spin-only' magnetic scaling factor, Φ_{so}, used to compare first-principles and experimental NMR parameters, was derived in a previous study by Kim et al.[10] from the Brillouin function in the low field, high temperature limit:

$$\Phi_{so}(\mathrm{T}) = \frac{B_0 {\mu_{\mathrm{eff}}}^2}{3k_{\mathrm{B}} g_{\mathrm{e}} \mu_{\mathrm{B}} S(T - \Theta)} \qquad \text{(S2)}.$$

B_0 is the external magnetic field strength, g_{e} is the free electron g–value, k_{B} is Boltzmann's constant, μ_{B} is the Bohr magneton, S is the formal spin of the transition metal species ($S_{\mathrm{Mn^{3+}}} = 2$), μ_{eff} is the effective magnetic moment per Mn site, T is the temperature of the sample, and Θ is the Weiss constant. An equivalent expression uses the temperature-dependent experimental (molar) magnetic susceptibility, $\chi_{\mathrm{m}}(T)$:

$$\Phi_{so}(\mathrm{T}) = \frac{B_0 \chi_{\mathrm{m}}(T)}{g_{\mathrm{e}} \mu_{\mathrm{B}} S N_{\mathrm{A}}} \qquad \text{(S3)},$$

where N_A is Avogadro's number. Equations (S2) and (S3) use 'spin-only' expressions for the magnetic moments, only strictly valid when the orbital angular momentum is quenched[25]. In other words, potential spin-orbit effects on the magnetic properties of the real sample are neglected.[10] Strong magnetic anisotropy and/or Zero-Field Splitting (ZFS) are reflected by substantial deviations of the g-value obtained on the real sample from the free electron g-value ($g_{\mathrm{e}} = 2.0023$). Spin-orbit coupling can be accounted for by re-scaling $\Phi_{\mathrm{so}}(\mathrm{T})$ by the ratio of the free electron g-value to the experimental g-value for $NaMnO_2$. The final expression for the scaling factor is:

$$\Phi(\mathrm{T}) = \Phi_{\mathrm{so}}(\mathrm{T})\frac{g_{\mathrm{e}}}{g} = \frac{B_0\chi_{\mathrm{m}}(T)}{g\mu_{\mathrm{B}}SN_{\mathrm{A}}} \qquad \text{(S4)}.$$

Here, a bulk molar susceptibility of 3.14×10^{-3} emu.mol^{-1} was obtained for the β-$NaMnO_2$ sample studied with NMR at 320 K (see MPMS data in Figure S3). To the best of our knowledge, no g-value has been reported for this material in the literature. The experimental g-value used here ($g = 1.993$) was taken from Zorko et al.'s ESR study of α-$NaMnO_2$,[19] and is expected to be similar to that of β-$NaMnO_2$. A bulk magnetic scaling factor $\Phi = 6.64\times10^{-3}$ was obtained at 320 K and at a 4.7 T external magnetic field. This value was used to compute the NMR parameters, the NMR measurements being performed on this sample.

4.2. Site-specific scaling factors from Monte Carlo simulations

4.2.a. Methodology and Experimental details

The code implements an Ising-type magnetic model for ions with spins, S, quantized in the direction of the external magnetic field, B_0, with spin magnetic moments $M_{\mathrm{S}} = -S, -S+1 \ldots S-1, S$. The Hamiltonian is of the form

$$H = -\mu B_0 \sum_i M_{\mathrm{S}} - \frac{1}{2}\sum_{<i,j>} J_a M_S^i M_S^j \qquad \text{(S5)},$$

where the first sum describes the interaction with the external magnetic field and the second sum accounts for the internal magnetic interactions between neighboring spins. J_a is the magnetic exchange energy between the ij ion pair and the factor of $1/2$ compensates for double counting.

Site-specific scaling factors for Mn spins in α-like, β-like nanodomains, and close to a twin boundary (Φ_α, Φ_β and Φ_{SF}, respectively) were obtained from Monte Carlo simulations on a supercell of Mixed Cell 1 (see Figure 2a in the main text) containing 960 Mn spins. Giot et al. found that in α-$NaMnO_2$ the correlation length along the major magnetic interaction, $J_{1\alpha}$, is approximately 30 Å at 50 K, but decreases on warming and plateaus at ca. 10 Å above 150 K.[18] Accordingly, the size of the Monte Carlo supercell along J_1 was set to 68.4 Å to capture long-range spin correlation effects in the simulations.

The simulations were initiated with the spins in an antiferromagnetic configuration at 400 K and the temperature of the heat bath was subsequently decreased in steps of 10 K, down to 320 K. An external magnetic field of 4.7 T was applied. The Metropolis algorithm was used to sample the spin configurational space and allow the system to equilibrate with the heat bath through a series of random single spin flips. 800 k Monte Carlo steps were performed at each temperature step and the cumulative spin configurations were saved every 100 k steps. The number of spin flips per Monte Carlo step was set to ten times the number of Mn spins in the supercell (i.e. 9600). The final spin configuration at temperature T served as the starting configuration for the following temperature step at T'=T-10 K. The number of initialization steps at the start of each temperature step was determined by the number of steps required for thermal equilibration of the system at 5 K (i.e. in the temperature regime where thermal equilibration is slow).

4.2.b. Why are site-specific scaling factors overestimated?

As mentioned in the main text of the paper, site-specific scaling factors obtained from the Monte Carlo simulations are systematically overestimated in comparison with the experimental bulk scaling factor. Possible reasons for these results were investigated and some were ruled out, as discussed below.

The J_a magnetic couplings obtained from calculations performed on the α-$NaMnO_2$[15] and β-$NaMnO_2$[16] experimental (EXP) structures, and on from the structures obtained after a first-principles optimization (OPT) are in close agreement. Therefore, the large *ab initio* scaling factors do not result from the structures used in the calculations.

System size effects were investigated by comparing the Φ_β values obtained from Monte Carlo simulations in three different β-$NaMnO_2$ supercells (and in Mixed Cell 1 for comparison), using a common (OPT H20) set of first-principles $J_{1\beta}, J_{2\beta}, J_{3\beta}$ magnetic couplings. The cell parameters, details of the Monte Carlo calculations, and Φ_β scaling factors at 320 K and 4.7 T are presented in Table S3.

System	# MC steps	# Mn	J_1 along	*a* / Å	*b* / Å	*c* / Å	α / °	β / °	γ / °	Φ_β
β-$NaMnO_2$	1 M	256	*ac*	21.90	25.17	21.90	90.0	62.7	90.0	7.12×10^{-3}
	800 k	1024	*ac*	43.81	25.17	43.81	90.0	62.7	90.0	7.27×10^{-3}
	700 k	960	*a*	85.77	27.81	19.14	90.0	90.0	65.7	7.22×10^{-3}
Mixed Cell 1	800 k	384 β-type	*a*	68.37	25.17	23.38	90.0	90.0	90.0	6.96×10^{-3}

Table S3. Structural parameters and Φ_β scaling factors of the different β-$NaMnO_2$ supercells (and Mixed Cell 1 for comparison) considered for the investigation of system size effects on the scaling factors obtained from Monte Carlo simulations. All Monte Carlo simulations were performed using a procedure similar to the one described in the experimental section of the paper for Mixed Cell 1. The number of Monte Carlo steps in the simulations (e.g. 1 M = 1,000 k steps) and the direction of the dominant $J_{1\beta}$ magnetic coupling the different supercells (*ac*: along the cell diagonal in the ac plane; *a*: along the *a* direction) are specified. All simulations were performed using the OPT H20 set of first-principles $J_{1\beta}, J_{2\beta}, J_{3\beta}$ magnetic couplings.

As shown in Table S3, the different β-$NaMnO_2$ supercell sizes lead to minimal changes in Φ_β at 320 K. $\Phi_{\beta\ computed}$ for Mixed Cell 1 is a little lower than those obtained on pure β-$NaMnO_2$, which may suggest that stacking faults have a small effect on the magnetic moments of Mn spins in β-$NaMnO_2$ domains. We conclude that system size effects are not at the origin of the overestimated Monte Carlo scaling factors in comparison to the experimental scaling factor.

5. Bond pathway decomposition analysis in α-$NaMnO_2$ and β-$NaMnO_2$

The bond pathway contributions (BPCs) to the total ^{23}Na Fermi contact shift, computed in the α-$NaMnO_2$ and β-$NaMnO_2$ structures, are presented in Figures 5a and 5b in the main text. The orbital interactions and spin density transfer mechanisms leading to the different P_i contributions are depicted in Figure S4 and discussed in more detail below.

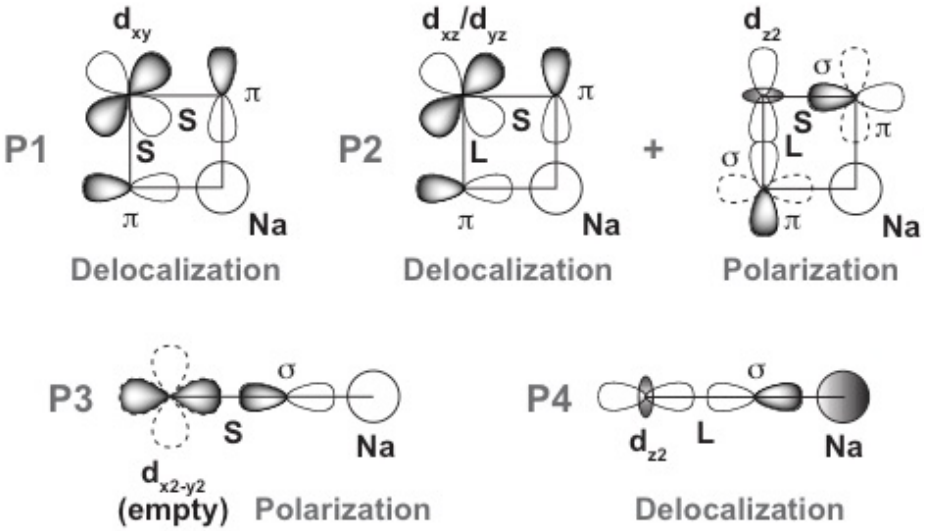

Figure S4. Orbital diagrams showing the Mn-O-Na hyperfine interaction pathways (P_i) contributing to the ^{23}Na Fermi contact (hyperfine) NMR shift in α- and β-$NaMnO_2$. The Mn-O bonds elongated by the Jahn-Teller effect are labeled with an L, and those shortened with an S. Angles deviate slightly from 90° and 180°, but this is not depicted in the orbital diagrams.

The sodium ions in α-$NaMnO_2$ are surrounded by twelve Mn^{3+} ions at the center of severely Jahn-Teller distorted MnO_6 octahedra, leading to a total of 18 Na^+-O-Mn^{3+} interactions, of which 12 are close to 90° and 6 are close to 180° (see Figure 5a in the main text). The nature of the Jahn-Teller distortion indicates that the d_z^2 orbital must be occupied and oriented along the direction of the elongated Mn-O bonds, while the unoccupied $d_{x^2-y^2}$ manganese orbital is oriented along the direction of the four shortened Mn-O bonds.

Focusing on the α-form first, the approximately 90° t_{2g}-O(π)-Na delocalization pathway in the xy plane (short Mn-O bonds), denoted P_1, leads to a strongly positive shift. The similar delocalization pathways in the xz and yz planes (albeit through one short and one long Mn-O bond), denoted P_2, are partially negated by the Hund's first rule type polarization of the O(π) orbitals due to strong d_z^2-O(σ) delocalization, resulting in an overall weakly negative shift. The shift due to the approximately 180° $d_{x^2-y^2}$(empty)-O(σ)-Na polarization (short Mn-O bonds), denoted P_3, is also weakly negative, as expected, while the approximately 180° d_z^2-O(σ)-Na delocalization (long Mn-O bonds), denoted P_4, is strongly positive, again as expected.

Each sodium in β-$NaMnO_2$ participates in 16 Na^+-O-Mn^{3+} interactions, of which 12 are close to 90° and 4 are close to 180° (see Figure 5b in the main text). In the β form, pathways P_1 and P_3 are split into two inequivalent but similar pathways labeled P_{1a} and P_{1b}, and P_{3a} and P_{3b}, respectively. The major difference between the hyperfine parameters of α- and β-$NaMnO_2$ is attributed to the lack of a P_4-type interaction in β-$NaMnO_2$. The bond pathway geometries in the α- and β-$NaMnO_2$ structures are presented in Tables S4a and S4b, respectively.

a) α-$NaMnO_2$				
Pathway geometry	d(Mn–Na) / Å	Mn–O–Na / °	d(O–Mn) / Å	d(Na–O) / Å
P_1 Mn^{3+}	3.15 (3.08)	94.8 (93.5)	1.96 (1.92)	2.31 (2.29)
P_2 Mn^{3+}	3.22 (3.11)	88.7 (86.3)	2.30 (2.27)	2.31 (2.29)
		92.3 (93.7)	1.96 (1.92)	2.47 (2.32)
P_3 Mn^{3+}	4.26 (4.20)	170.5 (170.6)	1.96 (1.92)	2.31 (2.29)
P_4 Mn^{3+}	4.78 (4.57)	168.9 (167.6)	2.30 (2.27)	2.47 (2.32)

b) β-$NaMnO_2$				
Pathway geometry	d(Mn–Na) / Å	Mn–O–Na / °	d(O–Mn) / Å	d(Na–O) / Å
P_{1a} Mn^{3+}	3.13 (3.12)	94.4 (94.2)	1.95 (1.91)	2.30 (2.33)
P_{1b} Mn^{3+}	3.21 (3.17)	95.3 (95.1)	1.92 (1.93)	2.40 (2.35)
P_2 Mn^{3+}	3.18 (3.18)	84.7 (85.0)	2.40 (2.35)	2.30 (2.35)
		93.9 (95.5)	1.92 (1.91)	2.41 (2.36)
P_{3a} Mn^{3+}	4.24 (4.23)	171.1 (169.4)	1.95 (1.91)	2.30 (2.33)
P_{3b} Mn^{3+}	4.30 (4.26)	168.3 (169.7)	1.92 (1.93)	2.40 (2.35)

Table S4. Mn-O-Na bond pathway geometries parameters for a) α-$NaMnO_2$, and b) β-$NaMnO_2$. Mn-O-Na pathway geometries are given in the H20 optimized (OPT) structures, and those in brackets in the experimental (EXP) structures of Parant et al.[15] and Hoppe et al.[16].

6. ^{23}Na NMR

6.1 Additional experimental details and assumptions made in the interpretation of the ^{23}Na NMR data

In this work, the observed ^{23}Na NMR shift is considered equal the sum of the hyperfine (Fermi contact) shift and of the second-order quadrupolar shift, as described by Equation (1) in the main text. The pseudo-contact shift, resulting from an anisotropic magnetic susceptibility tensor, is generally considered to be negligible in systems containing large hyperfine shifts.[26,27] Fits of the experimental data were performed using the SOLA lineshape simulation package within the Bruker Topspin software. Transverse (T_2') NMR relaxation times were obtained for

as-synthesized α- and β-$NaMnO_2$ from an exponential fit of the decay of the signal intensity obtained as the echo delay was increased in an NMR spin echo pulse sequence. Transverse relaxation times in the range of 2.5 to 4.0 ms were determined for the different Na environments in as-synthesised α- and β-$NaMnO_2$. These relaxation times are sufficiently long for the decay of the signal intensity over the signal acquisition time to be neglected.

6.2 Complementary ^{23}Na NMR data at 1 GHz

The spectrum obtained for as-synthesized β-$NaMnO_2$ at a magnetic field of 23.5 T is shown Figure S5. The isotropic shifts determined from a fit of the Na_β and Na_{SF} resonances in Figure 3a in the main text, obtained at a lower magnetic field of 4.7 T, are in good agreement with the peak positions of 316 and 510 ppm derived directly from the spectrum shown below, which is consistent with the fact that quadrupolar induced shifts (δ_{QIS}; see equation (1) in the main text) are negligible at very high field.

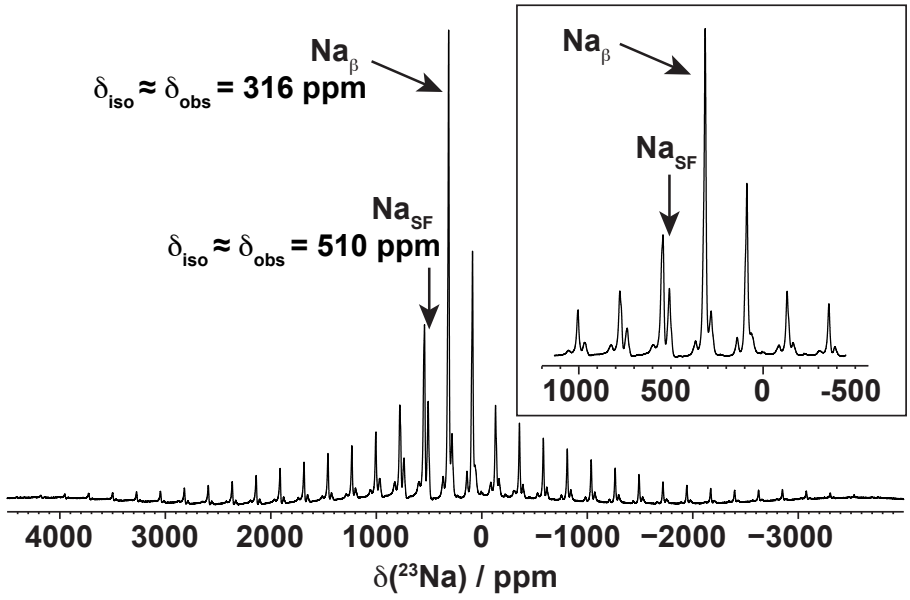

Figure S5. ^{23}Na NMR spectrum acquired on as-synthesized β-$NaMnO_2$ at room temperature on a Bruker Avance III 1000 spectrometer (23.5 T external magnetic field), at a Larmor frequency of –264.5 MHz. The NMR experiment was performed under 60 kHz magic angle spinning (MAS) using a 1.3 mm HX double-resonance probe. The chemical shift was referenced against solid ^{23}NaCl at 7.21 ppm. The ^{23}Na spin echo NMR spectrum was acquired using a 90° RF pulse of 0.83 μs and a 180° RF pulse of 1.66 ms at 245 W (300 kHz), and a recycle delay of 0.2 s. The centerbands of the Na_β and Na_{SF} NMR signals are indicated on the spectrum. An expanded view of the region containing the centerbands is shown in the inset.

References

(1) Becke, A. D. Density-functional thermochemistry. III. The role of exact exchange. *J. Chem. Phys.* **1993**, 98, 5648–5652.

(2) Lee, C.; Yang, W.; Parr, R. Development of the Colle-Salvetti correlation-energy formula into a functional of the electron density. *Phys. Rev., B Condens. Matter* **1988**, 37, 785–789.

(3) Vosko, S. H.; Wilk, L.; Nusair, M. Accurate spin-dependent electron liquid correlation energies for local spin density calculations: a critical analysis. *Can. J. Phys* **1980**, 58, 1200–1211.

(4) Stephens, P. J.; Devlin, F. J.; Chabalowski, C. F.; Frisch, M. J. Ab initio Calculation of Vibrational Absorption and Circular Dichroism Spectra Using Density Functional Force Fields. *J. Phys. Chem.* **1994**, 98, 11623–11627.

(5) Corà, F.; Alfredsson, M.; Mallia, G.; Middlemiss, D.; Mackrodt, W.; Dovesi, R.; Orlando, R. *Principles and Applications of Density Functional Theory in Inorganic Chemistry II*; Structure and Bonding 113; Springer: Berlin/Heidelberg, 2004, pp 171–232.

(6) Muscat, J.; Wander, A.; Harrison, N. M. On the prediction of band gaps from hybrid functional theory. *Chem. Phys. Lett.* **2001**, 342, 397–401.

(7) Feng, X.; Harrison, N. Magnetic coupling constants from a hybrid density functional with 35% Hartree-Fock exchange. *Phys. Rev. B* **2004**, 70, 092402.

(8) Middlemiss, D. S.; Lawton, L. M.; Wilson, C. C. A solid-state hybrid density functional theory study of Prussian blue analogues and related chlorides at pressure. *J. Phys.: Condens. Matter* **2008**, 20, 335231.

(9) de P R Moreira, I.; Illas, F.; Martin, R. Effect of Fock exchange on the electronic structure and magnetic coupling in NiO. *Phys. Rev. B* **2002**, 65, 155102.

(10) Kim, J.; Middlemiss, D. S.; Chernova, N. A.; Zhu, B. Y. X.; Masquelier, C.; Grey, C. P. Linking Local Environments and Hyperfine Shifts: A Combined Experimental and

Theoretical ^{31}P and ^{7}Li Solid-State NMR Study of Paramagnetic Fe(III) Phosphates. *J. Am. Chem. Soc.* **2010**, 132, 16825–16840.

(11) Middlemiss, D. S.; Ilott, A. J.; Clément, R. J.; Strobridge, F. C.; Grey, C. P. Density Functional Theory-Based Bond Pathway Decompositions of Hyperfine Shifts: Equipping Solid-State NMR to Characterize Atomic Environments in Paramagnetic Materials. *Chem. Mater.* **2013**, *25,* 1723–1734.

(12) Clément, R. J.; Pell, A. J.; Middlemiss, D. S.; Strobridge, F. C.; Miller, J. K.; Whittingham, M. S.; Emsley, L.; Grey, C. P.; Pintacuda, G. Spin-Transfer Pathways in Paramagnetic Lithium Transition-Metal Phosphates from Combined Broadband Isotropic Solid-State MAS NMR Spectroscopy and DFT Calculations. *J. Am. Chem. Soc.* **2012**, 134, 17178–17185.

(13) Dovesi, R.; Saunders, V. R.; Roetti, C.; Orlando, R.; Zicovich-Wilson, C. M.; Civalleri, B.; Pascale, F.; Doll, K.; Harrison, N. M.; Bush, I. J.; DArco, P.; Llunell, M. *Crystal09 user's manual*; University of Torino: Torino, Italy, 2010.

(14) Schäfer, A.; Horn, H.; Ahlrichs, R. Fully optimized contracted Gaussian basis sets for atoms Li to Kr. *J. Chem. Phys.* **1992**, 97, 2571–2577.

(15) Parant, J.-P.; Olazcuaga, R.; Devalette, M.; Fouassier, C.; Hagenmuller, P. Sur Quelques Nouvelles Phases de Formule Na_xMnO_2 ($x \leq 1$). *J. Solid State Chem.* **1971**, 3, 1–11.

(16) Hoppe, R.; Brachtel, G.; Jansen, M. Über $LiMnO_2$ und β-$NaMnO_2$. *Z. Anorg. Allg. Chem.* **1975**, 417, 1–10.

(17) Monkhorst, H. J.; Pack, J. D. Special points for Brillouin-zone integrations. *Phys. Rev. B* **1976**, 13, 5188–5192.

(18) Giot, M.; Chapon, L. C.; Androulakis, J.; Green, M. A.; Radaelli, P. G.; Lappas, A. Magnetoelastic Coupling and Symmetry Breaking in the Frustrated Antiferromagnet α-$NaMnO_2$. *Phys. Rev. Lett.* **2007**, 99, 247211.

(19) Zorko, A.; Shawish, El, S.; Arčon, D.; Jagličić, Z.; Lappas, A.; van Tol, H.; Brunel, L. Magnetic Interactions in α-$NaMnO_2$: Quantum spin-2 system on a spatially

anisotropic two-dimensional triangular lattice. *Phys. Rev. B* **2008**, 77, 024412.

(20) Stock, C.; Chapon, L. C.; Adamopoulos, O.; Lappas, A.; Giot, M.; Taylor, J. W.; Green, M. A.; Brown, C. M.; Radaelli, P. G. One-Dimensional Magnetic Fluctuations in the Spin-2 Triangular Lattice α-$NaMnO_2$. *Phys. Rev. Lett.* **2009**, 103, 077202.

(21) Abakumov, A. M.; Tsirlin, A. A.; Bakaimi, I.; Van Tendeloo, G.; Lappas, A. Multiple Twinning As a Structure Directing Mechanism in Layered Rock-Salt-Type Oxides: $NaMnO_2$ Polymorphism, Redox Potentials, and Magnetism. *Chem. Mater.* **2014**, 26, 3306–3315.

(22) Bakaimi, I.; Abakumov, A. M.; Green, M. A.; Lappas, A. Teherani, F. H.; Look, D. C.; Rogers, D. J. Crystal, Magnetic, and Dielectric Studies of the 2D Antiferromagnet: β-$NaMnO_2$. *Proc. SPIE*, **2014**, 898716.

(23) Franchini, C.; Podloucky, R.; Paier, J.; Marsman, M.; Kresse, G. Ground-state properties of multivalent manganese oxides: Density functional and hybrid density functional calculations. *Phys. Rev. B* **2007**, 75, 195128.

(24) Zhang, G. R.; Zou, L. J.; Zeng, Z.; Lin, H. Q. Magnetic and electronic properties of α-$NaMnO_2$. *J. Appl. Phys.* **2009**, 105, 07E512.

(25) Carlier, D.; Ménétrier, M.; Grey, C.; Delmas, C.; Ceder, G. Understanding the NMR shifts in paramagnetic transition metal oxides using density functional theory calculations. *Phys. Rev. B* **2003**, 67, 174103.

(26) Grey, C. P.; Lee, Y. J. Lithium MAS NMR studies of cathode materials for lithium-ion batteries. *Solid State Sci.* **2003**, 5, 883–894.

(27) Lee, Y. J.; Wang, F.; Grey, C. P. ^6Li and ^7Li MAS NMR Studies of Lithium Manganate Cathode Materials. *J. Am. Chem. Soc.* **1998**, 120, 12601–12613.